PAPER

Highly efficient photoluminescence of SiO₂ and Ce–SiO₂ microfibres and microspheres†

Juan M. Ruso,[a] A. Noel Gravina,‡[b] Noelia L. D'Elía‡[b] and Paula V. Messina*[b]

Semiconductor nanocrystals and nanostructures have been extensively studied in the last few years due to their interesting optical and optoelectronic properties. Nevertheless, combining precise photoluminescence properties with controlled morphologies of SiO₂ is a major hurdle for a broad range of basic research and technological applications. Here, we demonstrate that microemulsion droplet interfacial elasticity can be manipulated to induce definite morphologies associated with specific intrinsic and extrinsic photoluminescent defects in the silica matrix. Thus, under precise experimental conditions hollow crystalline and compact amorphous SiO₂ spheres showing ultraviolet-photoluminescence and helicoidal fibrils of Ce-doped amorphous silica with violet-blue emissions are obtained. Overall, it is demonstrated that the combination of microemulsions and doping represents an easy strategy for the design of specific nanoscale structures with high efficiency photoluminescence. The detailed structural analysis provided in the present work is expected to be useful as accurate information on assessment of technological nanostructures.

1. Introduction

Since the discovery of strong luminescence in silicon clusters at room temperature,[1] modern electronics has focused on silicon dioxide for the manufacture of optoelectronic devices, especially blue and ultraviolet (UV) luminescence devices. Several studies have addressed the problem of augmentation and stabilization of luminescence emission with different treatments, such as electron irradiation,[2] thermal treatment[3] and ion implantation.[4] Also significant effort has been devoted to the shape-controlled synthesis of semiconductor and metal oxide colloidal nanocrystals.[5] But it remains a challenge to create silicon materials possessing a specific morphological structure associated with defined photoluminescence emissions. Therefore, the development of synthetic methods for the preparation of complex micro- and nanostructured materials with tailored size and morphology is of great importance.[6–8] Among the strategies in use, based on bio-inspired morphogenesis, the synthesis *via* organized reaction environments is especially attractive to manipulate the nucleation and growth of complex inorganic materials.[9–11] In this regard, multiphase systems such as W/O microemulsions are thermodynamically stable with a continuous oil phase and compartmentalized aqueous domains covered by surfactant molecules, thus able to constrain and pattern the deposition of spatially confined inorganic precursors.[9] Particularly, the microemulsion-mediated hydrothermal method has been shown to be useful in the synthesis of a variety of 1-D nanostructures. Single-crystalline nanowires/nanorods of CdS,[12] BaF₂,[13] SnO₂,[14] AlPO₄-5,[15] and Ca₁₀(PO₄)₆(OH)₂[16] have been successfully obtained by reverse micelles under hydrothermal conditions. In previous work,[17] the authors successfully used a bottom-up anionic reverse microemulsion-based method as a nano-reactor to control the growth of 3D opal-CT materials with an unusual fibrous microstructure. Depending on the microemulsion template system, such materials also showed band gap values comparable to those obtained for silicon based metal oxide semiconductors and ultraviolet light photoluminescence (UV-PL).

Here, we have extended our study to evaluate different effects on the starting nano-reaction media in order to create a material with definite morphological characteristics associated with specific luminescent properties. Although all the aspects inherent to the microemulsion have been evaluated, we have focused on the effects of the microemulsion oil phase and the introduction of rare earth (RE) organic molecules on the interfacial rigidity and its impact on the material morpho-

[a]*Soft Matter and Molecular Biophysics Group, Department of Applied Physics, University of Santiago de Compostela, Santiago de Compostela, 15782, Spain*
[b]*Department of Chemistry, Universidad Nacional del Sur, INQUISUR-CONICET, (8000) Bahía Blanca, Argentina. E-mail: pmessina@uns.edu.ar; Fax: +54 291 4595160; Tel: +54 291 4595159*

†Electronic supplementary information (ESI) available: Material size distribution histograms; calcination temperature effect on materials (XRD characterization); characterization by XRD of Si–Ce1 material; characterization of CeO₂ nanoparticles (XRD, TEM), band gaps calculations and N₂ adsorption–desorption data. See DOI: 10.1039/c3dt32936d

‡Have the same participation in this work.

crystalline and photoluminescence properties of the SiO_2 matrix. Under specific experimental conditions, SiO_2 structures with definite morphologies and specific UV-A, UV-B and blue emission centers are created. The obtained result provides novel information on the complex process of UV-light emission in oxidized porous Si (OPS) and Si-nanostructures (SNS) and can address the new challenges evoked by the design of evolutionary devices applied for example in optical data storage.

2. Experimental

2.1 Materials

Hexadecyl-trimethyl ammonium bromide (CTAB, MW = 364.48 g mol^{-1}, 99% Sigma), isooctane (Merck, MW = 114.23 g mol^{-1}, δ = 0.688 g cm^{-3}), n-heptane (Merck, MW = 100.21 g mol^{-1}, δ = 0.684 g cm^{-3}), n-hexane (Merck, MW = 86.18 g mol^{-1}, δ = 0.6548 g cm^{-3}), cyclohexane (Merck, MW = 84.16 g mol^{-1}, δ = 0.776 g cm^{-3}), butyl alcohol (ButOH, Merck, MW = 74.12 g mol^{-1}, δ = 0.810 g cm^{-3}), cerium valerate ($Ce(Val)_3$, MW = 443.1 g mol^{-1}) and sodium tetraethyl orthosilicate (TEOS, Aldrich 98%) were used without further purification. For microemulsion preparation, only triple-distilled water was used.

2.2 SiO_2 synthesis

Experiments were performed on water/CTAB-ButOH/alkane microemulsion systems. The composition of the microemulsion is given in terms of weight fractions (wt%). Microemulsion systems of 16.76% of CTAB, 13.90% of 1-butanol, 59.29% of oil phase and 10.05% of aqueous phase were prepared using the injection method,[18] by mixing an appropriate quantity of water with a CTAB solution in oil. The resulting microemulsions were placed in Teflon-stoppered test tubes and aged for 24 h at 25 °C before use. Four microemulsion template systems were tested using isooctane, n-heptane, n-hexane and cyclohexane as the oil phase. As the critical micellization concentration (CMC) of CTAB in water[19] is low compared with the concentration used here, it can be presumed that all the surfactant molecules are localized at the interface between water and oil. To obtain the SiO_2 materials, 11.6 ml of TEOS were dissolved in 2 ml of water and stirred for 10 minutes at 500 rpm. Then, a solution of 1.1 g of NaOH in 20 ml of water was added drop-by-drop to the TEOS solution whilst stirring. A minute later, the above described microemulsion systems were poured into the mixture and stirred for 5 minutes. The resulting gels were left for 8, 15, and 24 h in an autoclave at 100 °C. The obtained materials were filtered, washed with triple-distilled water and left to dry at room temperature. Finally, they were calcined for 7 h at various temperatures from 500 °C to 800 °C in an air flux.

2.3 CeO_2–SiO_2 synthesis

For the synthesis of Ce–Si materials, the procedure was similar to the preparation of Si materials except for the dissolution of 1% of $Ce(Val)_3$ in ButOH before its incorporation into the microemulsion mixture.

2.4 CeO_2 nanoparticle synthesis

For CeO_2 nanoparticle synthesis two microemulsion systems were prepared: (i) microemulsion A containing 12.78% of CTAB, 9.58% of 1-butanol, 44.71% of oil phase, 31.93% of aqueous phase and 1% of $Ce(Val)_3$ and (ii) microemulsion B containing 12.78% of CTAB, 9.58% of 1-butanol, 44.71% of oil phase, 31.93% of aqueous phase and 1% of NaOH. The two stable microemulsions using the above compositions were mixed together using a magnetic stirrer for 1 h. The resulting microemulsion developed a yellowish hue, indicating the formation of CeO_2 nanoparticles, which were extracted by centrifuging at 10 000 rpm for 10 min. The CeO_2 nanoparticles were then washed with ethanol and stored as a dispersion in ethanol.

2.5 Field emission scanning electron microscopy (FE-SEM)

Field emission scanning electron microscopy (FE-SEM) was performed using a ZEISS FE-SEM ULTRA PLUS. Resolution: 0.8 nm at 30 kV; accelerating voltage: 0.02 V–30 kV (continuously adjusted in steps of 10 volts); magnification range 12–1 000 000×; sizes of openings: 7.5 μm, 10 μm, 20 μm, 30 μm, 60 μm and 120 μm. Local compensation of charge, by injecting nitrogen gas.

2.6 Transmission electron microscopy (TEM)

Transmission electron microscopy was performed using a Philips CM-12 transmission electron microscope equipped with a digital camera MEGA VIEW-II DOCU and operated at 120 kV with a magnification of 730 000×. High resolution transmission (H-TEM) microphotographs were taken using a Libra 200 FE OMEGA transmission electron microscope operated at 200 kV with a magnification of 1 000 000×. Observations were made in a bright field. Powdered samples were placed on copper supports of 2000 mesh.

2.7 X-ray powder diffraction

Powder X-ray diffraction (XRD) data were collected with a Philips PW 1710 diffractometer with Cu K_α radiation (λ = 1.5418 nm) and a graphite monochromator operated at 45 kV, 30 mA and 25 °C. Sample diffractograms were compared to the RUFF database:[20] R061107.9 for α-cristobalite, R090042.9 for orthorhombic α-tridymite and R050379-9 for cerianite.

2.8 UV-vis and fluorescence spectroscopy

The UV-vis and fluorescence absorption spectrum was recorded at 298 K by a UV-vis-NIR scanning spectrophotometer (Beckman, model DU 640) and a Varian Cary Eclipse spectrofluorometer respectively, using a 1 cm path length quartz cell. The spectrum was obtained for the Si1, Si2, Si–Ce1, Si–Ce2 materials and CeO_2 nanoparticles that had been sonicated in ethanol to yield homogeneous dispersions. Pure ethanol solution was used as a blank.

2.9 Nitrogen adsorption isotherms

The nitrogen adsorption isotherms at 77.6 K were measured with a Micrometrics Model Accelerated Surface Area and Porosimetry System (ASAP) 2020 instrument. Each sample was degassed at 373 K for 720 min at a pressure of 10^{-4} Pa.

3. Results and discussion

3.1 Synthesis conditions

3.1.1 Silicon oxide materials. Several factors should be considered carefully when selecting the appropriate synthesis conditions for a specific reaction in a reverse microemulsion system, since the composition of the microemulsion solution affects not only its stability but also the formation of nano-materials. Micelle formation by CTAB has been studied widely by several investigators. In the presence of oil, a co-surfactant (short-tailed alcohols) and water, CTAB molecules can form microemulsions. In our case, at low water content, aggregation of CTAB molecules in non-polar liquids has the inverse structure of aggregates in aqueous solution. Such aggregates present the polar heads packed together to form a central core surrounded by the hydrocarbon tails, which are often referred to as a reversed microemulsion, or a water-in-oil (W/O) microemulsion. Alcohol molecules are located between the hydrocarbon chains and near the polar heads of the surfactants. Water molecules are necessary to form reversed microemulsions and are located mainly in the polar core.[21] There are two types of water molecules in the interior of microemulsion droplets: (i) bound water, attached to the polar head group of surfactant molecules, and (ii) free water, referring to the bulk water inside the nano-droplet. According to the phase diagram of the pseudo-ternary system (water/CTAB-ButOH/oil),[22] we work within the isotropic fluid phase (L_2) where the structures of aggregates are only spheres. The dynamic nature of the reversed micelles plays a key role in the formation of the final morphology. This, in turn, is closely related to the rigidity of the nano-droplets oil–water interface. The film flexibility was increased by augmenting oil molecular weight (from cyclohexane to iso-octane[9]) approaching the instability boundary microemulsion conditions. Fig. 1 shows the SEM microphotographs of the four materials obtained by TEOS hydrolysis inside microemulsion droplets of different film rigidity, after hydrothermal treatment (100 °C, 24 h) and calcination (650 °C, 7 h) in an air flux. It can be seen that when cyclohexane or n-hexane were used as the oil phase, dense spheres of 0.7 and 2.5 µm diameter are obtained (Fig. 1a and 1b). Nevertheless, hollow spheres of 10.4 µm diameter are formed when the oil phase used in the template microemulsion is n-heptane (Fig. 1c). Size distribution histograms are shown in ESI.† Then, if the oil phase is changed to iso-octane a material with a nano-sheet structure is obtained (Fig. 1d and ESI†). All materials show perforations on their structures, however the analysis of N_2 adsorption–desorption data did not evidence the existence of a relevant porous structure or important surface area values (ESI†). So it was supposed that perforations
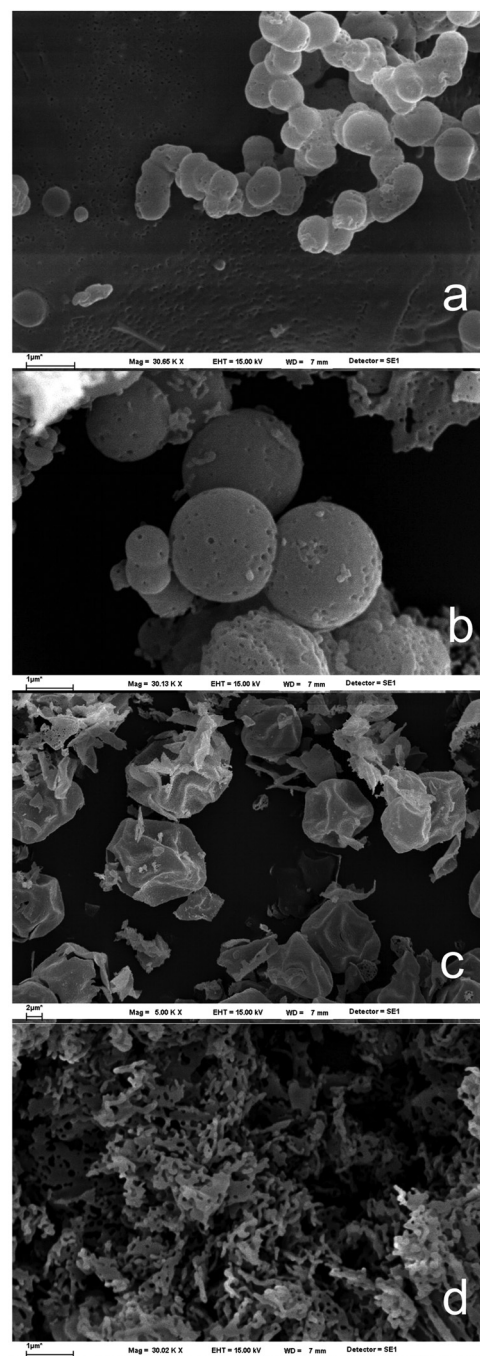

Fig. 1 SEM microphotographs of the SiO_2 materials obtained by TEOS hydrolysis inside (a) water/CTAB-ButOH/cyclohexane, (b) water/CTAB-ButOH/n-hexane, (c) water/CTAB-ButOH/n-heptane and (d) water/CTAB-ButOH/isooctane microemulsions.

are due to the sample degradation by electron beam incidence during microscopy observations.

To explain the different morphologies we must take into consideration that reactions involved in this silica synthesis include first the hydrolysis of TEOS and then the condensation (*i.e.*, polymerization) of hydrolyzed silica species (*i.e.*, monomeric and polymeric silica reacting units) in the presence of a base catalyst, NaOH. Formation of colloidal particles in W/O

microemulsions occurs not only through the polymerization of monomeric reactants into polymeric reacting species but also the subsequent polymerization of polymeric units into even larger ones. This polymerization process usually occurs through the dynamic fusion and fission of W/O microemulsion droplets which host reacting species and undergo incessant Brownian motion.[23] For those surfactant films with lower deformability or a stronger attachment to droplets, as happened when *n*-hexane or cyclo-hexane were used as the oil phase, interdroplet open water channels are less likely to occur for reacting species to pass through. With fewer interdroplet dynamic exchangers, reacting species tend to retain and grow in their respective droplets. TEOS hydrolysis involved both bound and free water inside nano-droplets leading to the formation of solid spheres of smaller size. When the film rigidity is decreased (by using *n*-heptane), the interdroplet exchange increases. Because the TEOS hydrolysis is rather slow[24] compared with the exchange of microemulsion droplet water contents, we supposed that the silica condensation involved only the bound water in the microemulsion interior. Free water molecules provide a means of hydrogen bonding between silica nuclei to sterically stabilize them in the oil continuum. In this case, bigger hollow spheres were obtained. By increasing a bit more the film flexibility, using iso-octane as the oil phase, an unfavorable larger deformation of surfactant film was achieved. The droplets coalesce and open water channels are likely to appear leading to microemulsion phase separation and a final nano-sheet structured material.

There is no direct correlation between the droplet size and the obtained sphere sizes.[24] To elucidate this, we have to take into account that in our case the synthesis is performed through a hydrothermal treatment. Essentially, under hydrothermal conditions, an oriented aggregation mechanism is usually adopted.[24] In the oriented aggregation mechanism, precipitation within spherical water droplets initially results in the formation of surfactant encapsulated primary nanoparticles which subsequently undergo oriented aggregation to induce the formation of inorganic crystal structures with dimensions considerably larger than the templates.[24] By subjecting the water/CTAB-ButOH/iso-octane microemulsion to the effects of hydrothermal treatment, reverse micelles are broken as shown in the oriented aggregation mechanism and due to their flexible interface the nano-droplets merge adopting a bicontinuous structure. When *n*-hexane, cyclohexane and *n*-heptane are used as an alternative to iso-octane, the nano-droplet films seem to be rigid enough to prevent the formation of interconnected channels. In light of the obtained results, it was found that the hydrothermal treatment is a crucial point in the synthesis of materials. Therefore, for those microemulsion systems giving rise to spheres different times of treatments were tested.

Fig. 2 shows the SEM microphotographs of materials obtained from water/CTAB-ButOH/cyclohexane, water/CTAB-ButOH/*n*-hexane and water/CTAB-ButOH/*n*-heptane template microemulsions after 8, 15 and 24 h of hydrothermal treatment. For all materials the number of spheres increases with
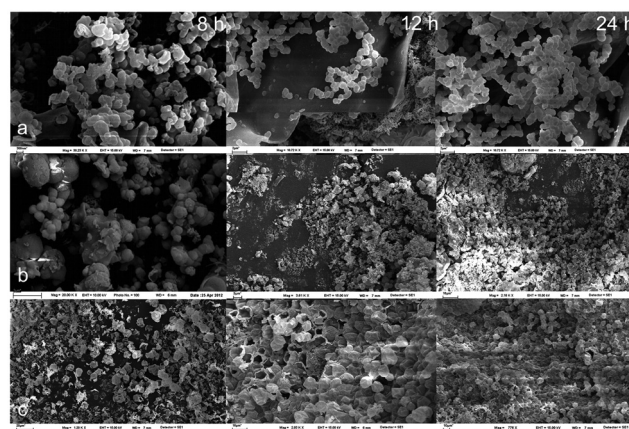

Fig. 2 SEM microphotographs of the SiO$_2$ materials obtained by TEOS hydrolysis inside (a) water/CTAB-ButOH/cyclohexane, (b) water/CTAB-ButOH/*n*-hexane, and (c) water/CTAB-ButOH/*n*-heptane after 8, 15 and 24 h of hydrothermal treatment.
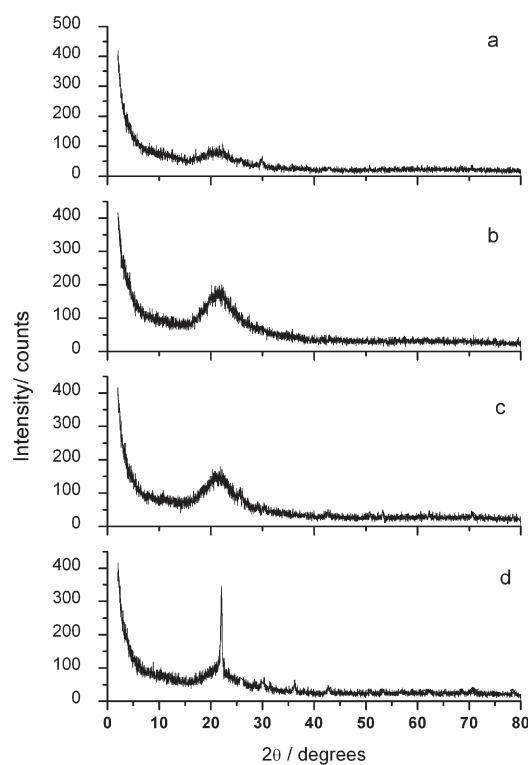

Fig. 3 X-ray diffraction patterns (XRD) of the SiO$_2$ materials obtained by TEOS hydrolysis inside (a) water/CTAB-ButOH/cyclohexane, (b) water/CTAB-ButOH/*n*-hexane, (c) water/CTAB-ButOH/*n*-heptane and (d) water/CTAB-ButOH/isooctane microemulsions.

the time of hydrothermal treatment while their dimensions are preserved. No differences in the material morphology were seen after 24 h of hydrothermal treatment.

Changes in the film rigidity also have a significant effect on materials microstructure, as we can appreciate from inspection of the materials X-ray diffraction patterns, Fig. 3. Only water/CTAB-ButOH/*n*-heptane template material presents
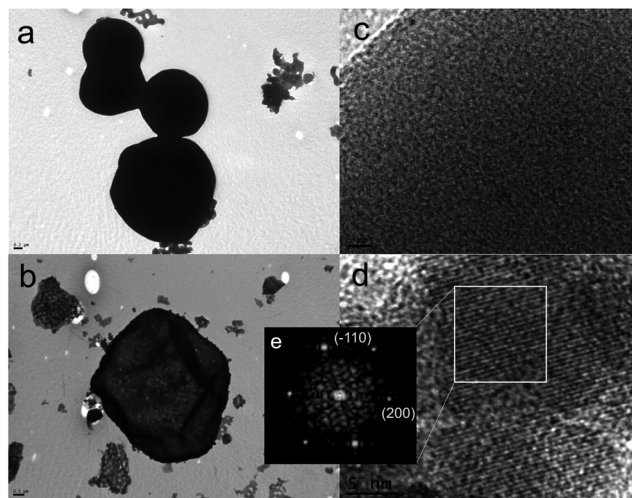
Fig. 4 TEM and H-TEM microphotographs of SiO$_2$ materials obtained by TEOS hydrolysis inside (a, c) water/CTAB-ButOH/n-hexane, (b, d) water/CTAB-ButOH/n-heptane microemulsions. (e) Cristobalite selected-area electron diffraction (SAED) patterns extracted from the Fourier transform (FFT) of H-TEM images by digitalized image processing.

crystallinity, denoting that SiO$_2$ crystal formation and growth requires a certain elasticity in the oil–water interface. The structure of the crystalline phase exhibits XRD patterns strongly resembling that of α-cristobalite with a slight broadening of the Bragg reflections. To distinguish between a poorly crystallized α-cristobalite phase and a kind of hydrous silica phase (opal-CT), we undertook a deep inspection of the material microstructure. The material does not present shifts to larger d-spacing that are characteristic of opal CT due to the presence of tridymite-type stacking faults in the [111] direction of the cristobalite three-layered structure.[25] The absence of stacking disorder was corroborated by high resolution transmission electron microscopy (H-TEM), Fig. 4d. We could also evidence the formation of cristobalite by the evaluation of the selected-area electron diffraction (SAED) patterns that can be extracted from the Fourier transform (FFT) of high resolution TEM images by digitalized image processing, Fig. 4e. The presence of a single set of Bragg reflections in the corresponding SAED pattern confirms the material crystalline nature. The results obtained for macroscopic ensembles of SiO$_2$ by using XRD and for microscopic segments of SiO$_2$ from the SAED patterns[26] are consistent with the presence of cristobalite.

Usually, the products obtained by alkoxide hydrolysis are amorphous or poorly crystallized, and subsequent calcinations are necessary to obtain the desired crystalline nanophase. The effect of calcination temperature was also evaluated. The X-ray diffraction patterns (XRD) of materials calcined at 500, 550, 650 and 800 °C were recorded (ESI†). Calcination has no effect on amorphous materials, denoting that crystal nuclei are formed during the hydrothermal treatment. For CTAB-ButOH/n-heptane template material, the decrease in the full width at half-maximum (FWHM) of peaks with increasing temperature indicates an increase of the material crystallinity. No

considerable differences were seen between the material calcined at 650 and 800 °C.

Those synthesis conditions that resulted in homogeneous amorphous solid (Si1) and partially crystalline hollow (Si2) spherical structured SiO$_2$ were then applied to the preparation of Ce-doped silicon oxide materials.

3.1.2 Cerium-doped silicon oxide materials. The solubility of optically active rare-earth ions in various silicon materials is universally low due to the mismatch of ionic radii and the strong covalent bonding of the matrix network.[27] It is recognized that it is very difficult to incorporate high concentrations of optically active rare-earths into silicon materials through equilibrium techniques such as the sol–gel method.[28] The incorporation of different proportions of Ce(Val)$_3$ into the microemulsion system was tested, verifying that more than 1% of Ce(Val)$_3$ destroy the microemulsion system. Otherwise, a lower amount of cerium may not have any effect on the material PL properties. The selected concentration of cerium was chosen based on a compromise between the stability of the emulsion and the optical properties of materials. Fig. 5 shows the SEM microphotographs of the obtained Si–Ce materials. It can be seen that a morphological transformation of pure silica materials occurred. Si1 material constituting dense spheres of about 2.5 μm in diameter is transformed into a helicoidally fibrillar structure material of more than 20 μm length and 0.5 μm in diameter. Nevertheless, the Si2 material with a hollow spherical structure ($d \approx 10.4$ μm) is changed to a small sized ($d \approx 1.2$ μm) solid spherical arrangement. The presence of Ce(Val)$_3$ bulkier groups modifies the packing parameter and, in turn, influences the radius of curvature of the microemulsion droplet in a way that causes an increase of the oil–water interface stiffness. It also manipulates the interfacial organization by affecting the compactness of the film and its temporal stability. There is experimental evidence that the addition of co-surfactants to ternary stable microemulsion
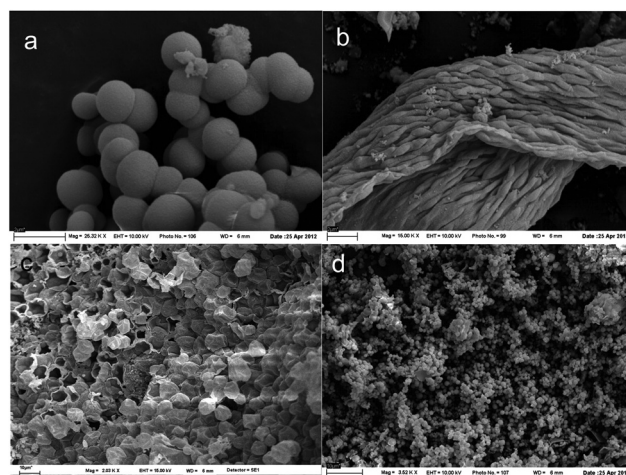

Fig. 5 SEM microphotographs of the SiO$_2$ and Ce-doped silica materials templated by (a) water/CTAB-ButOH/n-hexane, (b) water/CTAB-ButOH-Ce(Val)$_3$/n-hexane, (c) water/CTAB-ButOH/n-heptane and (d) water/CTAB-ButOH-Ce(Val)$_3$/n-heptane microemulsions.

systems has a similar effect.[29,30] In those cases the modification of the interfacial composition could drive variations in both the structure and the dimensions of the aggregates.[23] For an interfacial curvature $(1/R)$ we expect an energy contribution per unit area of the form[31]

$$F = \gamma - \frac{K}{R_0 R} + \frac{K}{2R^2} \qquad (1)$$

where γ is the interfacial tension, R_0 is the natural radius of curvature of a spherical micelle and R is the microemulsion droplet radius under given constraints (a given volume of water fraction ϕ_W and associated with n_S surfactants cm^{-3}).

Here $1/R_0$ is the spontaneous curvature and can be of either sign (positive when the trend is toward direct micelles). The parameter K has the dimension of energy and may be called the rigidity of the interface. The addition of a co-surfactant or any molecule that incorporates into the micro-droplet interface may act strongly on $1/R_0$ and also on K modifying the interfacial curvature energy contribution, F. We think that a similar effect is caused by the interfacial presence of Ce(Val)$_3$ molecules. It should be noted that this effect is of particular relevance in the systems under study because the CTAB can not form reverse micelles in alkanes without the assistance of a co-surfactant due to its unfavorable packing parameter. In both materials, no alteration of crystalline microstructure can be appreciated by ceria incorporation. Fig. 6 shows the XRD patterns of Si–Ce2 material. The silica microstructure is maintained, while new diffraction peaks resembling cerianite (CeO$_2$) appeared. The diffraction peaks observed show a good match with those of bulk cerium oxide. There is a considerable broadening of the peaks, suggesting that these particles are very small in dimension. Using the Scherrer formula,[32] the average size of the particles was estimated to be around 4.3 nm. Similar results were obtained for Si–Ce1 (ESI†). The observation of material microstructure by TEM (ESI†) revealed the presence of small particles of CeO$_2$ ($d \sim 5$ nm) in the bulk
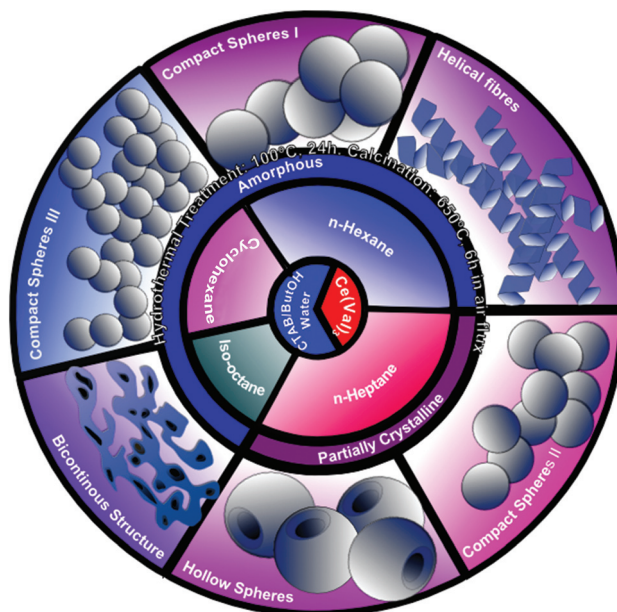
Scheme 1 Schematic representation of synthesis conditions and the resultant structures obtained.

of SiO$_2$ material. For comparison purposes, CeO$_2$ nanoparticles were prepared using the same microemulsion system in the absence of a silica precursor showing identical diameter and crystalline phase (ESI†). Similar results were found in the literature.[33] The final synthesis conditions and the morphological and microstructural properties of the different prepared materials are summarized in Scheme 1.

3.2 Photoluminescence

Structural, optical and electrical properties in silica materials can be dramatically changed by manipulating the presence of defects in the silica matrix. Such defects are classified according to their structure and size (point defects), dislocations (linear defects) and plane defects; they can be induced by tuning the material manufacturing process. In the previous section we have shown how the synthesis procedure can be altered to fabricate materials of different morphology and microstructure. Here we examined how the applied synthesis conditions induce intrinsic and extrinsic point defects on the silica matrix that are responsible for their ultraviolet photoluminescence (PL) properties.

3.2.1 Intrinsic point defects. Intrinsic point defects involve atoms of the host matrix only, *i.e.* vacancies (the host atoms are missing) and self-interstitials (additional host atoms at an interstitial position).[34] In order to elucidate the energy structure of the luminescent defects and to better understand the mechanisms responsible for their radiative relaxation, we measured the PL and PL excitation spectra at room temperature. Fig. 7a and 7b show adsorption and PL emission spectra of poorly crystalline SiO$_2$ material (Si2). Both adsorption and emission spectra were deconvoluting into a sum of Gaussian shapes. The adsorption spectrum is dominated by

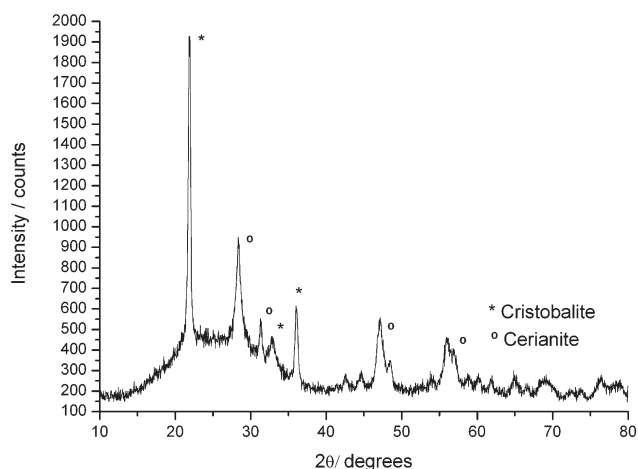**Fig. 6** X-ray diffraction patterns (XRD) of the spherical Ce-doped crystalline silica material templated by a water/CTAB-BuOH-Ce(Val)$_3$/n-heptane microemulsion.
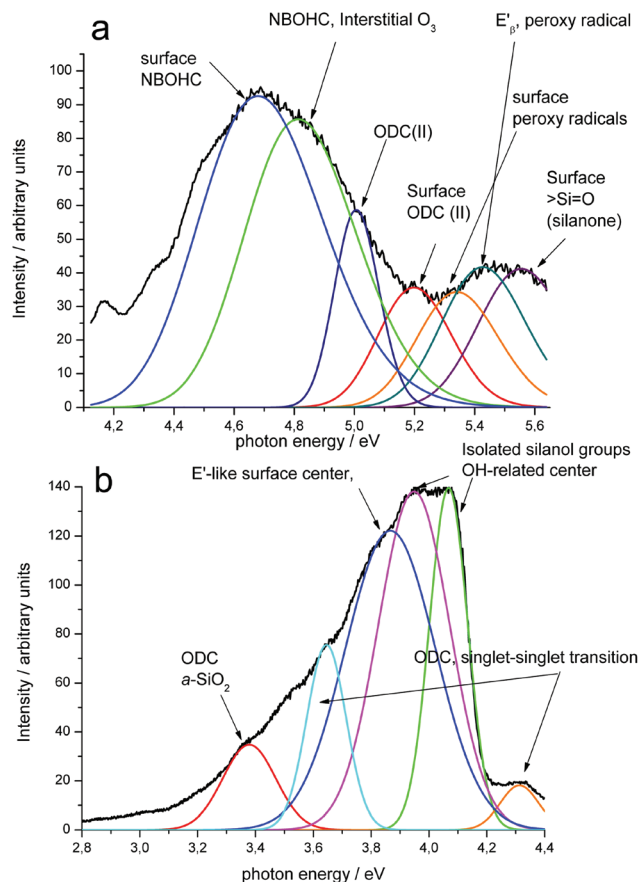
Fig. 7 Photoluminescent (a) absorption and (b) emission of Si1 material. Similar results were obtained for Si2 material.

two high intensity bands centered at 4.6 and 4.8 eV that can be assigned to the presence of surface and bulk NBOHC (non-bridging oxygen hole center) and interstitial O_3. The NBOHC defect can be visualized as the oxygen part of a broken bond. It is electrically neutral and paramagnetic and represents the simplest elementary oxygen related intrinsic defect in silica. The most unique fingerprint of this centre is the 1.9 eV luminescent band in the red region of the visible light spectra. Moreover, in the gas phase, O_2 dissociated into two atomic oxygens (2O) at $h\nu > 5.1$ eV, the same can be expected to occur in silica glass following a photolytic reaction.[34] The atomic oxygen appearing as a result of this reaction might be expected to be relatively mobile in silica even at room temperature; then they can interact with other oxygen molecules to form ozone (O_3) as occurs in the earth's atmosphere. It is believed that O_3 molecules are responsible for both the 4.8 eV absorption and the 1.9 eV luminescence in certain oxygen-rich silicas, which usually is attributed to the NBOHC by many authors.[34,35] By inspection of PL emission spectra, it can be appreciated that emission bands peaking at 1.9 eV characteristic of the above mentioned point defects are not present. Nevertheless there are two intense bands centered at 3.9 and 4.1 eV that correspond to isolated silanol and OH-related centers.

Silanol and OH-related centers can be produced by a recombination of NBOHC or interstitial oxygen with hydrogen-related defects. Hydrogen is used to passivate the silicon or oxygen dangling bonds in the SiO_2 network and is often incorporated unintentionally into SiO_2. This passivation also decreases the number of non-bridging oxygens. Since it is commonly found in silicon dioxide, some authors[34,35] considered hydrogen to be an intrinsic defect (H(I) center, $\equiv$Si–H·, $\equiv$Si–Si·Si$\equiv$) with absorption bands at 4.8–6 eV and not registered PL emission. This group can act simultaneously as an electron and a hole trap.

Other bands of minor intensity are identified in absorption spectra with their correspondent PL emissions; those are assigned to different diamagnetic oxygen-deficiency centers (ODC) most commonly denoted as a neutral oxygen vacancy (ODC(I)) and two fold coordinated silicon denoted as $\equiv$Si·· (ODC(II)), and paramagnetic E′ centers. The ODC(I) represents one of the essential defects in all silicon dioxide modifications in the form of simple oxygen vacancies; here two Si atoms could relax and form a silicon–silicon bond (relaxed oxygen vacancies, $\equiv$Si–Si$\equiv$) or stay in unstable interaction conditions and form an unrelaxed oxygen vacancy ($\equiv$Si$\cdots$Si$\equiv$). Each one of them could be a precursor for the other under some circumstances and both are considered as key in many defect-type generations and transformations in the silica matrix. The 7.6 eV absorption band has been ascribed to the ODC(I).[35] This band is absent in our materials absorption spectra, while two PL bands at 4.4 eV and 2.7 eV have been observed under excitation at 5 eV. Such bands indicate the interaction of ODC(II) with ODC(I). Based on their lifetimes, the 4.4 eV and 2.7 eV bands have been attributed to singlet–singlet ($S_1 \rightarrow S_2$) and triplet–singlet ($T_1 \rightarrow S_0$) transitions. The origin of ODC(II) associated with the optical absorption band at 5 eV is still a matter of controversy. The first model hypothesis suggested that ODC(II) is a neutral diamagnetic oxygen vacancy, later two other models described the ODC(II) as twofold coordinated silica or an unrelaxed oxygen vacancy. The oxygen vacancy model was further supported by the finding that two-photon photobleaching of SiODC(II) generates E′-centers.[34] By an inspection of Si1 material spectra we can note the presence of absorption and emission bands of low intensity centered at 5.4 eV and 3.8 eV respectively that can be assigned to E′-like centers. These findings support the oxygen vacancy model for generation of the ODC(II) defect in our materials. Four main types of E′ centers, labeled E'_{α}, E'_{β}, E'_{γ}, E'_{s}, have been identified in vitreous silica.[34] The absorption band centered around 5.4 eV is signaled as characteristic of the E'_{β} defect. In the silica network E'_{β} features a proton trapped in the oxygen vacancy and the silicon atom contains the unpaired spin relaxed outwards, *i.e.*, the interaction of the unpaired spin associated with a long-bond silicon with the hydrogen atom is weak enough to not saturate each other. The presence of such a defect also supports our previous assumption related to the presence of H defects.

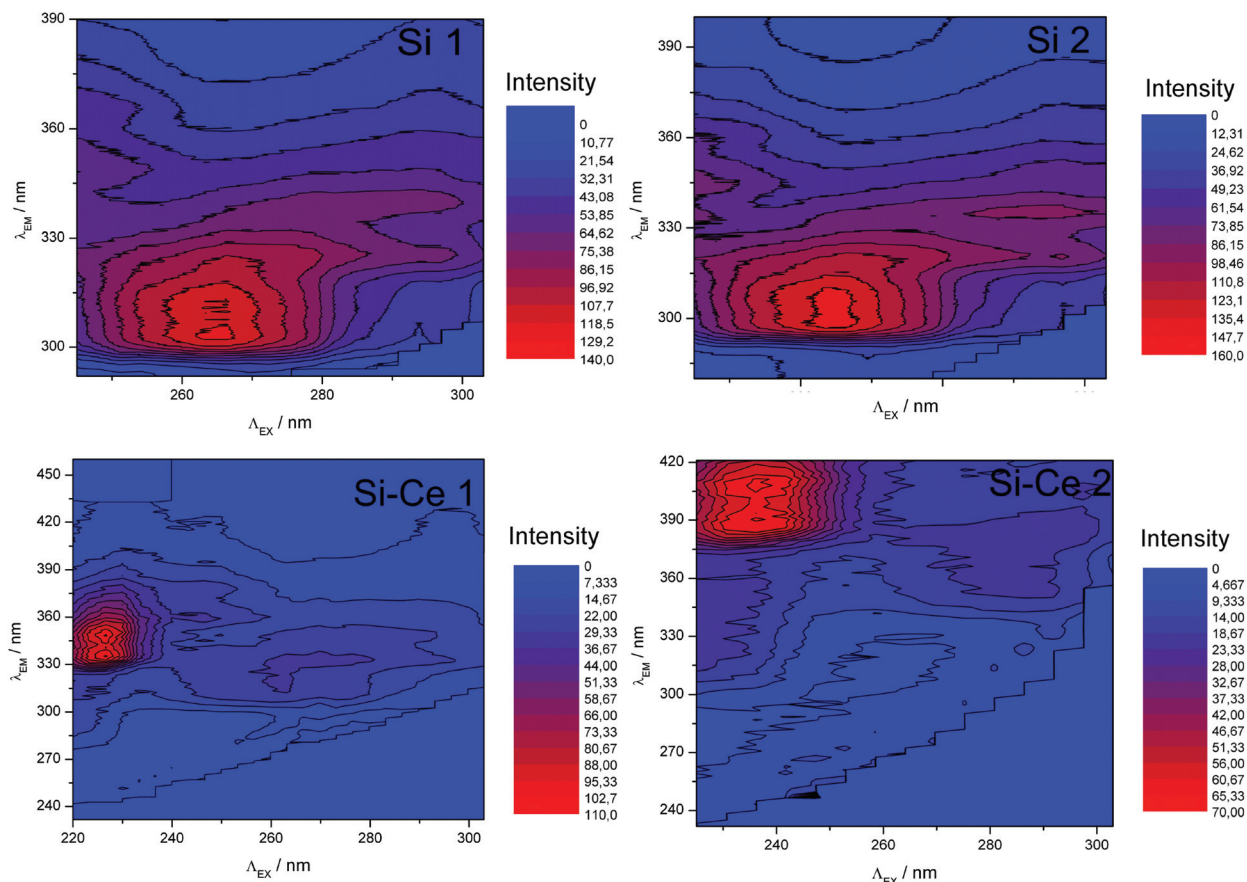The shape of the emission spectra is sensitive to the photon excitation energy as we can appreciate from the

Fig. 8 PL–PL excitation (PLE) patterns of the compact amorphous SiO₂ spheres (Si1), the hollow crystalline SiO₂ spheres (Si2), helicoidally fibrillar Ce-doped amorphous silica (Si–Ce1) and compact spherical Ce-doped crystalline silica (Si–Ce2) at room temperature.

inspection of the PL–PL excitation (PLE) patterns of the compact amorphous SiO_2 spheres (Si1) and the hollow crystalline SiO_2 spheres (Si2) at room temperature, Fig. 8a and 8b. This suggests the presence of overlapped levels in the material rather than one specific defect with a well-localized energy level. In spite of material crystallinity both PLE profiles present a similar absorption–emission pattern. This is due to the fact that short-range order defects in the silicate structure are determined mainly by silicon–silicon and silicon–oxygen interactions rather than by interactions between oxygen atoms.[34] Nevertheless, the effect of the amorphous state goes beyond merely introducing isotropy and the inhomogeneous broadening effects: it provides new structural degrees of freedom for defect formation. Defects whose properties are determined in the first order by interactions within a single SiO_4 tetrahedron like dangling-bond type defects, NBOHC, E′-like surface centers and ODC(II) cannot occur in pure crystalline material due to the steric limitation, such defects seem to be peculiar to the glassy state only.[35] The manifestation of such defects in both tested materials indicates the prevalence of amorphous phase effects over crystalline ones.

3.2.2 Extrinsic point defects. Extrinsic point defects involve atoms chemically different from the host crystal, such as those used for electric doping. Fig. 9 shows the room-
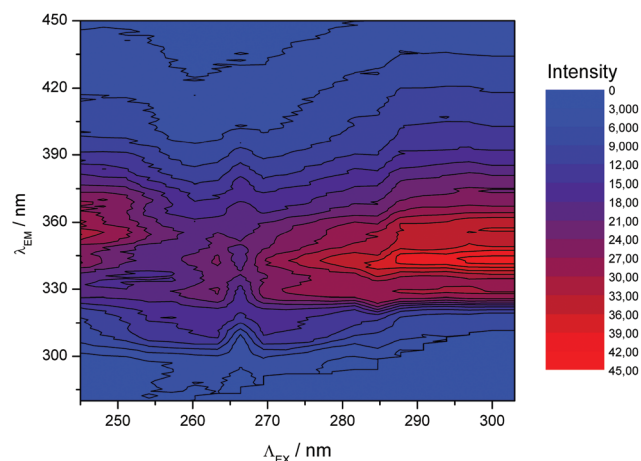

Fig. 9 PL–PL excitation (PLE) patterns of CeO₂ nanoparticles.

temperature PLE profile of CeO_2 nanoparticles. It is dominated by maximum emissions at 345 nm (3.65 eV) and 360 nm (3.44 eV) when exciting in the 287–300 nm (4.13–4.32 eV) range. The UV light peaks at 360 nm and 345 nm are the usual ones observed[36] in CeO₂ materials and could be explained by charge transitions from the 4f band to the valence band of

CeO_2. CeO_2 is a wide band gap semiconductor, whose calculated gap is about 3.37 eV (ESI†); it is easy to observe the hopping from Ce 4f to O 2p (exciting at $h\nu \geq 3$ eV). In addition, the defect levels localized between Ce 4f and O 2p can result in wider emission bands. Cerium can exist in both trivalent and tetravalent forms by losing two 6s electrons and either one or two 4f electrons. Ce^{4+} is optically inactive due to the lack of 4f electrons. As the materials were prepared under oxygen rich conditions, most of the Ce ions are quadrivalent and possibly in the form of CeO_2. Since Ce^{4+} ions are the dominant species in the prepared samples only a few optically active Ce^{3+} ions exist, so the corresponding emission intensity is low.

Fig. 8c and 8d show the PLE maps for both prepared Ce doped silica crystalline and amorphous materials at room temperature. The PL emissions of both samples mismatch with the emissions of the previously analyzed SiO_2 and CeO_2 materials. All emissions have higher intensity and a narrower range of λ_{EX} than the CeO_2 materials, probably due to an increase of the Ce^{3+}/Ce^{4+} ratio. The major point is the displacement of PL bands at minor λ_{EX}; only significant PL emissions were obtained by exciting at $h\nu \geq 5$ eV. Here the effect of the amorphous and crystalline phase is considerable, *i.e.*, fibrillar Ce-doped amorphous silica material (Si–Ce1) shows a broad PL peak at 3.63 eV (341 nm), Fig. 8d, while the Ce-doped crystalline silica compact spheres (Si–Ce2) show two PL bands centered at 3.02 eV (410 nm) and 2.50 eV (495 nm), Fig. 8c.

For Ce-doped amorphous silica material we supposed that both Ce^{3+} ions and radiative oxide defects could be responsible for the emission bands. Defects, including oxygen vacancies in the CeO_2 crystal with electronic energy levels below the 4f band, possibly act as radiative recombination centers for electrons initially excited from the valence band to the 4f band of the oxide. This claim is consistent with an enhanced adsorption tail below 3 eV in nonstoichiometric CeO_2 that was observed and attributed to the presence of oxygen vacancies.[37] Luminescence from optically active rare-earth ions is mainly attributed to their intra 4f or 5d–4f transitions. Intra-4f transitions are relatively independent of the host material, since the 4f states are shielded from outside interaction by 5d states. Although the 4f states are shielded by 5s and 5p states, the 5d states into which the 4f electron will be excited are exposed to the surrounding ligands. Because the most remarkable effect in the amorphous Ce-doped materials is that the PL emission shifts towards lower regions of excitation wavelength, we suppose that the resultant emission for Ce-doped silica material is related to the exposure and the consequent alteration of Ce 5d states to the nearby silica defects. Different from what happened with silica amorphous material, the presence of Ce atoms on partially crystalline SiO_2 causes the disappearance of the original UV-PL to give rise to Vis-PL. This would be probably due to a luminescence quenching through ion–ion interactions or by forming an optically inactive phase.[25] Probably, the crystalline SiO_x matrix forms a more uniform and stable structure to solubilized Ce atoms and accordingly the Ce^{3+} ions form clusters. As a consequence, the corresponding emissions from the Ce^{3+} ions are quenched by transferring their energy to other Ce^{3+} ions in the vicinity.[38]

4. Conclusions

In the above study, we have verified that micro-droplet interfacial rigidity can be manipulated to induce simultaneously a specific morphology and photoluminescent intrinsic defects on the SiO_2 matrix. Thus, hollow crystalline (Si1) and compact amorphous (Si2) SiO_2 spheres were created by sodium tetraethyl orthosilicate hydrolysis inside water/CTAB-ButOH/ *n*-heptane and water/CTAB-ButOH/*n*-hexane nanodroplets after 24 h of hydrothermal treatment at 100 °C and 7 h of calcination at 650 °C in an air flux. In spite of the phase crystallinity (α-cristobalite or amorphous respectively), the tested SiO_2 materials show similar main luminescence bands. Their PLE profiles are dominated by the emission centered at the UV-B (λ_{EM} = 306 nm, 4.05 eV) and UV-A (λ_{EM} = 326 nm, 3.80 eV) region which were assigned to the existence of OH-related and E′-like surface emitting centers. Other less relevant emissions occurred due to the presence of oxygen deficient centers (ODC). The intercalation of $(Val)_3Ce$ molecules on the microreactor structure gave rise to a morphological change and new PL properties. As a result, hollow and amorphous compact silica spheres were transformed into Ce-doped silica materials with compact spherical (Si–Ce1) and helical fibrillar (Si–Ce2) structures respectively. Furthermore, the presence of Ce-atoms on the silica matrix causes the displacement of PL bands at shorter excitation wavelengths, so that only significant PL emissions were obtained by exciting at $h\nu \geq 5$ eV. The fibrillar Ce-doped amorphous silica material showed UV-A photoluminescence ascribed to the exposure and the consequent alteration of Ce 5d states (into which the Ce 4f electron will be excited) to the nearby silica defects. Such interactions induce a high intensity narrow emission denoting the miscibility of optically active rare-earths in the silicon network. Compact spherical Ce-doped crystalline silica material showed blue emissions at 390 and 404 nm, in this case it was inferred that the SiO_x matrix forms a more uniform and stable structure to solubilized Ce atoms, resulting in the formation of Ce^{3+} clusters. As a consequence, the corresponding emissions from the Ce^{3+} ions are quenched by transferring their energy to other Ce^{3+} ions in the vicinity. Our work has the potential to stimulate a lot of attention on Si-based light emitting devices applied to integrated optoelectronics. In addition, the concept of shape-directed photoluminescence might be a pathway towards new opportunities in fields such as photodynamic therapy or plasmonic metamaterials for biosensing.

References

1 M. A. Green, J. Zhao, A. Wang, P. J. Reece and M. Gal, *Nature*, 2001, **412**, 805–808.

2 M. A. Stevens-Kalceff, *Phys. Rev. Lett.*, 2000, **84**, 3137–3140.

3 T.-W. Lee and O. O. Park, *Appl. Phys. Lett.*, 2000, **77**, 3334–3336.

4 P. Pellegrino, A. Perez-Rodriguez, B. Garrido, O. Gonzalez-Varona, J. R. Morante, S. Marcinkevicius, A. Galeckas and J. Linnros, *Appl. Phys. Lett.*, 2004, **84**, 25–27.

5 L. Han, P. Xiong, J. Bai and S. Che, *J. Am. Chem. Soc.*, 2011, **133**, 6106–6109.

6 X. Guo, Y. Deng, B. Tu and D. Zhao, *Langmuir*, 2009, **26**, 702–708.

7 N. Y. He, S. X. Ge, C. Yang, J. M. Cao and M. Gu, *Mater. Lett.*, 2004, **58**, 3304–3307.

8 D. Kong, C. Zhang, Z. Xu, G. Li, Z. Hou and J. Lin, *J. Colloid Interface Sci.*, 2010, **352**, 278–284.

9 L. Qi, in *Encycl. Surf. Coll. Sci.*, Taylor & Francis., 2006, pp. 6183–6207.

10 F. C. Meldrum and H. Coelfen, *ChemInform*, 2009, **40**, 4332–4432.

11 A. K. Ganguli, T. Ahmad, S. Vaidya and J. Ahmed, *Pure Appl. Chem.*, 2008, **80**, 2451–2477.

12 S. Q. Sun and T. Li, *Cryst. Growth Des.*, 2007, **7**, 2367–2371.

13 M. Cao, C. Hu and E. Wang, *J. Am. Chem. Soc.*, 2003, **125**, 11196–11197.

14 D. F. Zhang, L. D. Sun, J. L. Yin and C. H. Yan, *Adv. Mater.*, 2003, **15**, 1022–1025.

15 M. Z. Yates, K. C. Ott, E. R. Birnbaum and T. M. McCleskey, *Angew. Chem., Int. Ed.*, 2002, **41**, 476–478.

16 M. Cao, Y. Wang, C. Guo, Y. Qi and C. Hu, *Langmuir*, 2004, **20**, 4784–4786.

17 N. Hassan, V. Verdinelli, J. M. Ruso and P. V. Messina, *Langmuir*, 2011, **27**, 8905–8912.

18 P. Alexandridis, J. F. Holzwarth and T. A. Hatton, *Langmuir*, 1993, **9**, 2045–2052.

19 C. Yang, F. Chen, S. Luo, G. Xie, G. Zeng and C. Fan, *J. Hazard. Mater.*, 2010, **175**, 187–192.

20 http://rruff.info/

21 F. Li, G.-Z. Li, H.-Q. Wang and Q.-J. Xue, *Colloids Surf., A*, 1997, **127**, 89–96.

22 G. Palazzo, F. Lopez, M. Giustini, G. Colafemmina and A. Ceglie, *J. Phys. Chem. B*, 2003, **107**, 1924–1931.

23 C.-L. Chang and H. S. Fogler, *Langmuir*, 1997, **13**, 3295–3307.

24 K. Osseo-Asare and F. J. Arriagada, *J. Colloid Interface Sci.*, 1999, **218**, 68–76.

25 A. Ilieva, B. Mihailova, Z. Tsintzov and O. Petrov, *Am. Mineral.*, 2007, **92**, 1325–1333.

26 L. Zhao, N. Li, A. Langner, M. Steinhart, T. Y. Tan, E. Pippel, H. Hofmeister, K. N. Tu and U. Gösele, *Adv. Funct. Mater.*, 2007, **17**, 1952–1957.

27 A. J. Kenyon, *Prog. Quantum Electron.*, 2002, **26**, 225–284.

28 A. Vedda, N. Chiodini, D. Di Martino, M. Fasoli, M. Martini, A. Paleari, G. Spinolo, M. Nikl, N. Solovieva, A. Baraldi and R. Capelletti, *Phys. Status Solidi C*, 2005, **2**, 620–623.

29 H. T. Jung, B. Coldren, J. A. Zasadzinski, D. J. Iampietro and E. W. Kaler, *Proc. Natl. Acad. Sci. U. S. A.*, 2001, **98**, 1353–1357.

30 M. L. Curri, A. Agostiano, L. Manna, M. D. Monica, M. Catalano, L. Chiavarone, V. Spagnolo and M. Lugarà, *J. Phys. Chem. B*, 2000, **104**, 8391–8397.

31 P. G. De Gennes and C. Taupin, *J. Phys. Chem.*, 1982, **86**, 2294–2304.

32 P. Mohapatra, T. Mishra and K. M. Parida, *Appl. Catal., A*, 2006, **310**, 183–189.

33 F. Grasset, R. Marchand, A. M. Marie, D. Fauchadour and F. Fajardie, *J. Colloid Interface Sci.*, 2006, **299**, 726–732.

34 R. Salh, in *Crystalline Silicon: Properties and Uses*, ed. S. Basu, InTech, Rijeka, 2011, pp. 135–172.

35 L. Skuja, *J. Non-Cryst. Solids*, 1998, **239**, 16–48.

36 H. Gu and M. D. Soucek, *Chem. Mater.*, 2007, **19**, 1103–1110.

37 A. H. Morshed, M. E. Moussa, S. M. Bedair, R. Leonard, S. X. Liu and N. El-Masry, *Appl. Phys. Lett.*, 1997, **70**, 1647–1649.

38 H Bi, W. Cai, H. Shi, B. Yao and L. Zhang, *J. Phys. D: Appl. Phys.*, 2000, **33**, 2369–2372.